Wiley Analytical Science

Virtual Conference

The 5th edition of the Wiley Analytical Science Conference starts November 8, 2022!

Featured Sessions:

- **Integration of X-ray microscopy and finite elements into a digital twin**

  Thurs Nov 10, 10:00 - 10:30 AM EST / 4:00 - 4:30 PM CET

- **Optimization of Cryo TEM lamella preparation workflows to be faster and more accessible**

  Wed Nov 16, 10:00 - 11:00 AM EST / 4:00 - 5:00 PM CET

events.bizzabo.com/WASconferenceFall2022

ZEISS
Seeing beyond

TESCAN
PERFORMANCE IN NANOSPACE

WILEY

Check for updates

ADVANCED MATERIALS
www.advmat.de

High-Rate and Selective CO_2 Electrolysis to Ethylene via Metal–Organic-Framework-Augmented CO_2 Availability

Dae-Hyun Nam, Osama Shekhah, Adnan Ozden, Christopher McCallum, Fengwang Li, Xue Wang, Yanwei Lum, Taemin Lee, Jun Li, Joshua Wicks, Andrew Johnston, David Sinton, Mohamed Eddaoudi,* and Edward H. Sargent**

High-rate conversion of carbon dioxide (CO_2) to ethylene (C_2H_4) in the CO_2 reduction reaction (CO_2RR) requires fine control over the phase boundary of the gas diffusion electrode (GDE) to overcome the limit of CO_2 solubility in aqueous electrolytes. Here, a metal–organic framework (MOF)-functionalized GDE design is presented, based on a catalysts:MOFs:hydrophobic substrate materials layered architecture, that leads to high-rate and selective C_2H_4 production in flow cells and membrane electrode assembly (MEA) electrolyzers. It is found that using electroanalysis and operando X-ray absorption spectroscopy (XAS), MOF-induced organic layers in GDEs augment the local CO_2 concentration near the active sites of the Cu catalysts. MOFs with different CO_2 adsorption abilities are used, and the stacking ordering of MOFs in the GDE is varied. While sputtering Cu on poly(tetrafluoroethylene) (PTFE) (Cu/PTFE) exhibits 43% C_2H_4 Faradaic efficiency (FE) at a current density of 200 mA cm^{-2} in a flow cell, 49% C_2H_4 FE at 1 A cm^{-2} is achieved on MOF-augmented GDEs in CO_2RR. MOF-augmented GDEs are further evaluated in an MEA electrolyzer, achieving a C_2H_4 partial current density of 220 mA cm^{-2} for CO_2RR and 121 mA cm^{-2} for the carbon monoxide reduction reaction (CORR), representing 2.7-fold and 15-fold improvement in C_2H_4 production rate, compared to those obtained on bare Cu/PTFE.

1. Introduction

Electrochemical carbon dioxide reduction reaction (CO_2RR), powered by renewable electricity, is a promising route to achieve net-zero emissions for the production of chemicals and fuels.[1–3] Due to the similar thermodynamic reductive potential range for chemical formation in CO_2RR, C_1 and C_2 chemicals are usually generated simultaneously, resulting in poor selectivity. To achieve economically compelling CO_2RR, technoeconomic analysis (TEA) highlights the pressing need for industrially relevant productivity (>200 mA cm^{-2}) and energy efficiency (>50%) for CO_2 to ethylene (C_2H_4) conversion.[4,5] This emphasizes the importance of high selectivity, high energy efficiency, and high product yield.[4–9] There exists an urgent need to find electrocatalysts and reactors enabling to produce a specific chemical efficiently at a low cost.

Understanding the CO_2RR electrolyzer is crucial for this purpose. In an H-cell, CO_2 is bubbled into the electrolyte and the low CO_2 solubility limits the production rates of C_2H_4 to several tens of mA cm^{-2} in CO_2RR.[10] In the flow cell, where catholyte, anolyte, and CO_2 flow independently in separate chambers, CO_2 gas is supplied from the backside of a porous gas diffusion electrode (GDE), overcoming the mass transport limitation and achieving C_2H_4 productivities of >100 mA cm^{-2}.[11] Membrane electrode assembly (MEA) electrolyzers are newly emerging systems, where cathode:membrane:anode are stacked together to minimize ohmic loss.[12,13]

Electrocatalysts are deployed typically on hydrophobic and porous substrates to form GDEs. The design of GDEs is important to achieve efficient transport of CO_2 to the local reaction environment.[14,15] Three mass transport regions, which include the electrolyte phase reaction (bulk reaction), reaction

D.-H. Nam, F. Li, X. Wang, Y. Lum, J. Wicks, A. Johnston, E. H. Sargent
Department of Electrical and Computer Engineering
University of Toronto
10 King's College Road, Toronto, Ontario M5S 3G4, Canada
E-mail: ted.sargent@utoronto.ca
D.-H. Nam, T. Lee
Department of Energy Science and Engineering
Daegu Gyeongbuk Institute of Science and Technology (DGIST)
333 Techno jungang-daero, Daegu 42988, Republic of Korea

The ORCID identification number(s) for the author(s) of this article can be found under https://doi.org/10.1002/adma.202207088.

DOI: 10.1002/adma.202207088

O. Shekhah, M. Eddaoudi
Division of Physical Sciences and Engineering
Advanced Membranes and Porous Materials Center
Functional Materials Design
Discovery and Development Research Group (FMD3)
King Abdullah University of Science and Technology (KAUST)
Thuwal 23955–6900, Kingdom of Saudi Arabia
E-mail: mohamed.eddaoudi@kaust.edu.sa
A. Ozden, C. McCallum, J. Li, D. Sinton
Department of Mechanical and Industrial Engineering
University of Toronto
5 King's College Road, Toronto, Ontario M5S 3G8, Canada
E-mail: sinton@mie.utoronto.ca

 © 2022 Wiley-VCH GmbH

15214095, 0, Downloaded from https://onlinelibrary.wiley.com/doi/10.1002/adma.202207088 by University Of Toronto Libraries, Wiley Online Library on [16/11/2022]. See the Terms and Conditions (https://onlinelibrary.wiley.com/terms-and-conditions) on Wiley Online Library for rules of use; OA articles are governed by the applicable Creative Commons License

at double-phase boundary of catalyst–electrolyte (DPB, surface reaction), and reaction at triple phase region of catalyst–electrolyte–gas (TPR, triple phase region) can affect the CO_2RR of GDEs according to current density and pore size.[16,17] For example, ionomer as gas transport channel for active site is required for efficient electroreduction of carbon monoxide (CORR) at GDE because of poor CO solubility in aqueous electrolyte.[14] For CO_2RR, achieving a strict control on the local CO_2 availability, i.e., through CO_2-absorbing porous materials placed underneath the catalyst layer, could be key to suppress the competing hydrogen evolution reaction (HER) and achieve high reaction rates in CO_2-to-C_2H_4 conversion.

In the last three decades, metal–organic frameworks (MOFs) as a new crystalline porous material have emerged and gained remarkable attention in light of their unique properties. MOFs, constructed from metal-containing nodes linked by organic ligand bridges, have well-defined crystallographic and geometric microporous structures.[18] MOFs are designed, synthesized, and tuned using various approaches, enabling facile optimization of their pore structures and surface functions making them versatile. Recently, due to the higher CO_2 storage capacity of MOFs—based on physical adsorption—relative to traditional porous materials, MOFs are one of the widely used porous materials in carbon capture technologies.[19]

Many MOFs are applied to selectively adsorb gases benefiting from the molecular sieving effect, suggesting only the molecules with suitable pore kinetic diameters pass through the pores. This gas-selective diffusion is also driven by the differences in affinities/interactions among the frameworks and the targeted probe molecules, where the structure and chemical functionality of the pores are variable on the length of organic linkers, functionalization, and integration of coordinative unsaturated metal sites, etc. Recently, we have successfully deployed a molecular-building-block approach and isoreticular chemistry to synthesize various analogs of special class of fluorinated MOFs. These MOFs include $[M^1(M^2F_x)_2(L)_2]_n$ family, which is based on diverse organic ligands (L) like pyrazine, metal nodes (M^1) like Cu^{2+}, and pillars (M^2F_x) like SiF_6^{2}. Many of these fluorinated MOFs have shown exceptional properties for CO_2 capture and separation.[20–23] Their excellent gas separation performance is associated with their crystal structures consisting of square lattice layers (sql) of metal nodes and organic linkers. These layers are pillared by fluorinated anions that generate a 3D coordination framework with a primitive cubic (pcu) topology and the resultant MOF exhibits uniformly distributed adsorption energetics sites. Isoreticular chemistry enables us to alter the structural pore-aperture size by controlling the length and functional groups of organic linkers along with the natures of both the metal nodes and the pillars.[24] These MOFs can be easily tuned to enhance the adsorption energetics and hence achieve high CO_2 uptake and selectivity even at very low partial pressures relevant to air capture.

Recently, we studied the size effect of pore-aperture on gas separation by studying adsorption properties of MOFs.[24] We discovered a new gas-separation concept based on kinetics and thermodynamics that leads to selective CO_2 adsorption.[24] These materials perform better at CO_2 adsorption since the physisorption mechanism of the adsorbents requires much lower regeneration energy. Accordingly, we postulate that this MOF platform's ability to selectively adsorb CO_2 makes it an excellent candidate to be employed as an underlayer to preconcentrate CO_2 in the local reaction environment and eventually achieve high CO_2RR productivities.

In this work, we focus on harnessing MOFs in GDE to maintain high CO_2 concentration near the catalytically active sites, and thereby achieve high-rate and selective CO_2RR. We investigated the effect of MOF-augmented GDE on the extension of current density range for selective C_2H_4 production. We investigated two types of Cu-based MOFs (HKUST-1 and **SIFSIX**-Cu-3) with different CO_2 gas adsorption affinity and capacity. Operando X-ray absorption spectroscopy (XAS) study enabled investigation of the MOF stability during CO_2RR. We successfully verified the effect of MOF layer on enhancing C_2H_4 productivity of CO_2RR in flow cell and CO_2RR/CORR in MEA electrolyzer systems.

In previous reports, CO_2RR studies of Cu-based MOFs applied MOFs as active materials and as templates to fabricate porous carbon with Cu species. In Cu-based MOFs used as active materials, previous reports focused on Cu reconstruction in MOFs and resultant control over selectivity to methane (CH_4) and C_2H_4.[25–29] For CO_2RR using a GDE in a flow cell, nanostructured Cu with controlled size, shape, and oxide-derived Cu strategies were investigated.[30–33] Cu alloys and molecularly enhanced Cu increased selectivity to C_2H_4.[34–36] Recently, studies of GDE structures including hybrids with a polymer layer, ionomers, and PTFE, have been reported to enhance CO_2 mass transport.[14,37,38] To enhance CO_2RR stability, MEA electrolyzers have received recent attention, and strategies for Cu active materials design have focused on C_2H_4 production.[12,39–42] To the best of our knowledge, MOF-augmented GDEs that enable CO_2RR at high current density represent a new topic for investigation:[43–46] we explored whether MOF-induced local CO_2 concentration control can enhance CO_2 availability and thus aid in achieving high-rate C_{2+} product formation and overcoming mass transport limitations in CO_2RR.

2. Results and Discussion

We fabricated MOF-sandwiched multilayer GDEs by forming a highly porous and continuous MOF layer between Cu active materials and hydrophobic poly(tetrafluoroethylene) (PTFE). In contrast with carbon paper-based GDEs, PTFE prevents flooding of the electrolyte and electrowetting. Since HER dominates following flooding, it is desirable to maintain hydrophobicity during CO_2RR.[14,47,48] This GDE design enabled us to study the role of MOF in the preconcentration of CO_2 near the catalytically active sites. In the flow cell, catholyte and anolyte are circulated in independent compartments, and CO_2 gas is supplied to the active materials from the backside of the GDE (**Figure 1**a). In our GDE configuration, CO_2 gas directly flows from the back side of the PTFE through the MOF underlayer to reach the catalytically active sites (Figure 1b). The MOFs were deposited on the PTFE substrate, and Cu layer with 300 nm thickness was sputtered on top of the MOF layer for CO_2RR at the flow cell (Figure 1c). If the Cu thickness is too thin, the electrical conduction is hindered by the rough surface of the MOF layer on polymer-based PTFE. If the Cu is too thick,

© 2022 Wiley-VCH GmbH

15214095, 0, Downloaded from https://onlinelibrary.wiley.com/doi/10.1002/adma.202207088 by University Of Toronto Libraries, Wiley Online Library on [16/11/2022]. See the Terms and Conditions (https://onlinelibrary.wiley.com/terms-and-conditions) on Wiley Online Library for rules of use; OA articles are governed by the applicable Creative Commons License

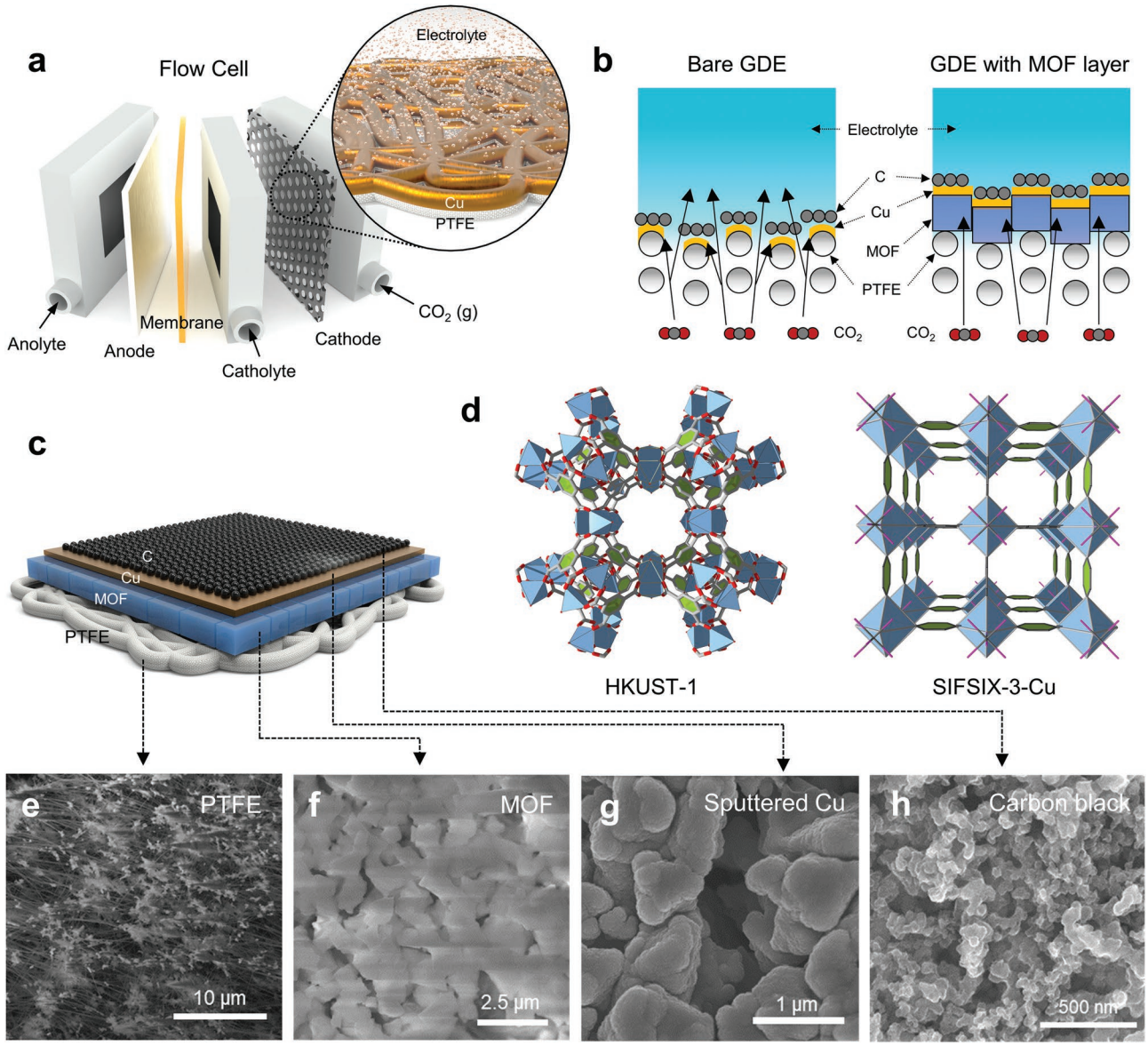

Figure 1. Fabrication of MOF-augmented GDE for electrochemical CO_2RR. a) Components of the flow cell for CO_2RR. b) Cross-sectional schematic diagram of bare GDE (Cu/PTFE) and MOF-augmented GDE (Cu/MOF/PTFE) during CO_2RR in the flow cell. c) Schematic of MOF-augmented GDE components (C/Cu/MOF/PTFE). d) Structures of HKUST-1 and **SIFSIX**-3-Cu MOFs for capturing the CO_2 in the cathode. e–h) SEM images of PTFE (e), the MOF layer (f), sputtered Cu (g), and carbon black (h), which show surface morphology according to the electrode fabrication step.

it will be difficult to apply the MOF underlayer effect to the CO_2RR of sputtered Cu. We then deposited a carbon (C) layer by spray coating carbon black powder-dispersed ink onto the Cu layer of the GDE to perform the role of current collector.[47] The thickness of C layer was ≈7 µm (Figure S1, Supporting Information).

We used two types of MOFs as HKUST-1 (Figure S2, Supporting Information),[25,49] namely $Cu_3(btc)_2.xH_2O$ (btc = benzene-1,3,5-tricarboxylate) with moderate CO_2 affinity and **SIFSIX**-3-Cu (Figure S3 and S4, Supporting Information)[20] which has a higher affinity and can selectively adsorb and store CO_2 in its pores (Figure 1d). To optimize the coordinatively unsaturated open metal sites in the secondary building unit (SBU), the synthesized MOF was dehydrated by thermal treatment.[49] The activation temperatures were chosen according to thermogravimetric analysis (TGA) of the MOFs.[20,25] Because abrupt thermal decomposition of HKUST-1 initiates at 300 °C, we calcined HKUST-1 at 250 °C for 3 h and sought to preserve the structural integrity of HKUST-1 during dehydration and carboxylate group decoupling near Cu dimer.[25] **SIFSIX**-3-Cu was activated by thermal treatment at 100 °C for 1 h. Plane-view scanning electron microscopy (SEM) images revealed the successful deposition of each layer (Figure 1e–h). Thus, in such a GDE, gaseous CO_2 transports to the catalytically active sites through the CO_2-selective MOF underlayer. In the carbon layer/sputtered Cu/PTFE (C/Cu/PTFE) GDE, we found that Cu was sputtered on the PTFE homogeneously and continuously covered the fibers (Figure S5, Supporting Information).

 © 2022 Wiley-VCH GmbH

15214095, 0, Downloaded from https://onlinelibrary.wiley.com/doi/10.1002/adma.202207088 by University Of Toronto Libraries, Wiley Online Library on [16/11/2022]. See the Terms and Conditions (https://onlinelibrary.wiley.com/terms-and-conditions) on Wiley Online Library for rules of use; OA articles are governed by the applicable Creative Commons License

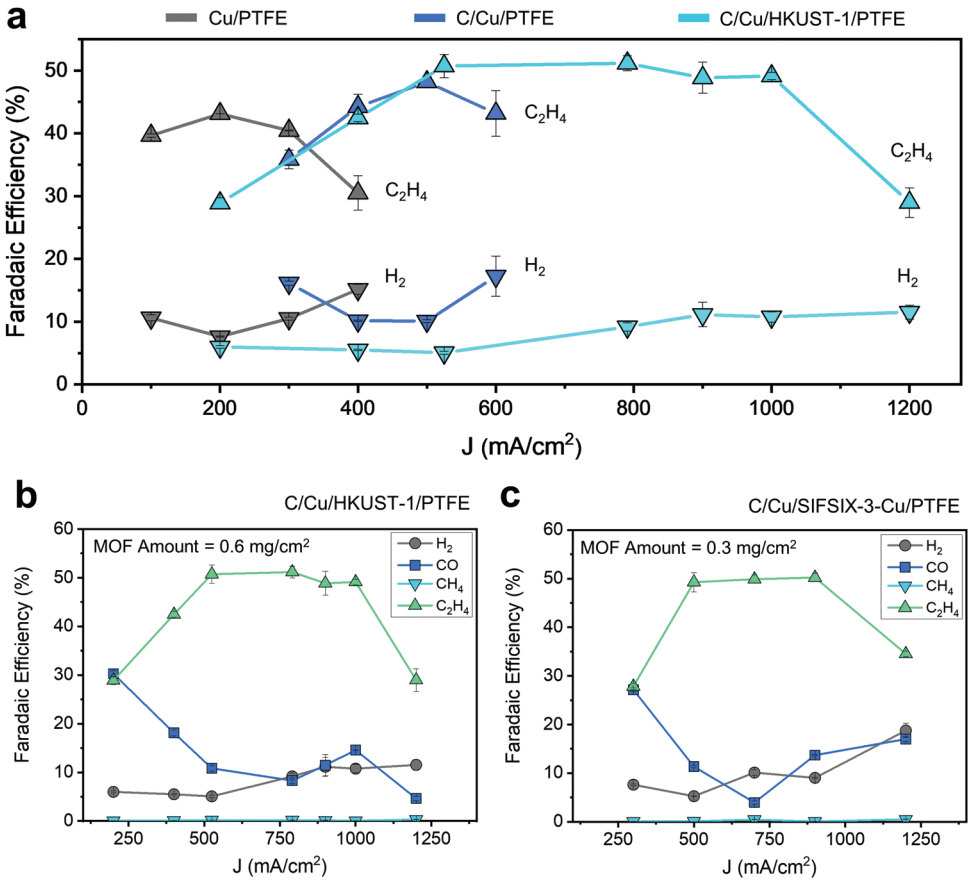

Figure 2. Electrochemical CO_2RR of MOF-augmented GDE in the flow cell. a) Comparison of C_2H_4 and H_2 product selectivities of Cu/PTFE, C/Cu/PTFE, and C/Cu/HKUST-1/PTFE according to the current density in 1 M KOH electrolyte. b,c) Effect of MOF type on the CO_2RR of MOF-augmented GDE electrode in 1 M KOH electrolyte: b) C/Cu/HKUST-1/PTFE (MOF amount: 0.6 mg cm^{-2}), and c) C/Cu/**SIFSIX**-3-Cu/PTFE (MOF amount: 0.3 mg cm^{-2}).

Maintaining the original structures of the MOFs during the GDE fabrication is essential to utilize selective gas permeability of MOFs for CO_2RR. We investigated the crystallinity of the MOF-augmented GDE using X-ray diffraction (XRD) analysis to track the MOF stability (Figure S6, Supporting Information). Sputtered Cu exhibited Cu (111) and (200) crystalline peaks at 43.6° and 50.7°. We also found XRD peaks for (220) and (222) of HKUST-1 at 9.6° and 11.8° in Cu/HKUST-1/PTFE. This reveals the preservation of MOFs during the deposition of Cu catalyst and C adlayer. Grain-incidence wide-angle X-ray scattering (GIWAXS) also shows the uniform alignment of HKUST-1 on the PTFE substrate upon deposition of Cu catalyst and C adlayer (Figure S7, Supporting Information). **SIFSIX**-3-Cu-augmented GDE was fabricated in the same way with HKUST-1-augmented GDE.

To investigate the effect of MOF on underlayer-augmented local CO_2 concentration, we compared the CO_2RR performances of Cu/PTFE, C/Cu/PTFE, and C/Cu/MOF/PTFE at various current densities in a flow cell (**Figure 2**). On Cu/PTFE, C_2H_4 Faradaic efficiency (FE) with a peak value of 43% was obtained at −0.84 V (vs RHE) with a current density of 200 mA cm^{-2} (Figure 2a, Figure S8a, Supporting Information). As the current density increased to 400 mA cm^{-2}, C_2H_4 FE decreased to 31% and H_2 FE increased to 15% (H_2 FE at 200 mA cm^{-2} = 7.6%), indicating that the conventional GDEs suffer from lack of CO_2 availability even at a moderate reaction rate (200 mA cm^{-2}).[14,16] The C_2H_4 partial current density was capped at around 122 mA cm^{-2}.

When the carbon adlayer composed of carbon black and perfluorosulfonic (PFSA) acid ionomer (Nafion) was deposited on the Cu/PTFE, C_2H_4 FE at 400 mA cm^{-2} increased to 44% whereas C_2H_4 FE on Cu/PTFE decreased to 30%. C_2H_4 FE on C/Cu/PTFE increased from 36% to 48% and C_2H_4 partial current density reached 241 mA cm^{-2} when the current density increased from 300 to 500 mA cm^{-2}. At the current density of 600 mA cm^{-2}, C_2H_4 FE decreased to 43% and H_2 FE increased to 17%. Enhanced CO FE at a lower potential range is attributed to the carbon adlayer, and the generated *CO was further reduced to C_2H_4 with the increase of applied potential (Figure S8b, Supporting Information).[4,47] Furthermore, the PFSA ionomer has extra channels, through which CO_2 gas transports to the catalytically active sites.[14] The PFSA-ionomer augmented CO_2 availability in C/Cu/PTFE extends the current density range for C_2H_4 formation compared to Cu/PTFE, consistent with our previous work.[14]

We noted a dramatic increase in the C_2H_4 partial current density when calcined-HKUST-1 is sandwiched between the sputtered Cu and PTFE (Figure 2a). Unlike GDEs without MOF layer, the C_2H_4 FE increased from 43% to 51% as the current density increased from 400 to 525 mA cm^{-2} with an H_2 FE of

© 2022 Wiley-VCH GmbH

15214095, 0, Downloaded from https://onlinelibrary.wiley.com/doi/10.1002/adma.202207088 by University Of Toronto Libraries, Wiley Online Library on [16/11/2022]. See the Terms and Conditions (https://onlinelibrary.wiley.com/terms-and-conditions) on Wiley Online Library for rules of use; OA articles are governed by the applicable Creative Commons License

only 5% in the C/Cu/HKUST-1/PTFE (MOF mass loading = 0.6 mg cm^{-2}). The GDE maintained C_2H_4 FEs above 48% up to a current density of 1 A cm^{-2} at –1.3 V (vs RHE) with a C_2H_4 partial current density of 491 mA cm^{-2}. Nearly 2-fold enhancement of C_2H_4 production rate on C/Cu/HKUST-1/PTFE compared to C/Cu/PTFE shows the merit of improved local CO_2 concentration for facilitating high-rate CO_2RR.[50] When as-synthesized HKUST-1 was placed between sputtered Cu and PTFE, the C_2H_4 production rate degraded as the current density increased over 200 mA cm^{-2}, and the C_2H_4 FE was below 25% at 400 mA cm^{-2} (Figure S8c, Supporting Information). This can be explained by increased HER obtained using as-synthesized HKUST-1.[25] This reveals that HKUST-1—MOF underlayer—boosts the production rates toward C_2H_4 by leveraging the locally improved CO_2 availability.

We studied the effect of mass loading of MOF underlayer on the C_2H_4 selectivity under different current densities (Figure 2b, Figure S9a and S9b, Supporting Information). When the mass loading of HKUST-1 was 0.3 mg cm^{-2}, we noted a CO_2RR gaseous product distribution similar to that of C/Cu/PTFE (Figure S9a, Supporting Information). However, when the mass loading of MOF was 0.6 mg cm^{-2}, we observed the extension of the current density to 1 A cm^{-2} for stable C_2H_4 production (Figure 2b). Compared to Cu/PTFE, C/Cu/PTFE, and C/Cu/HKUST-1 (0.3 mg cm^{-2})/PTFE, we noted a promoted CO FE of 30% at 200 mA cm^{-2} on C/Cu/HKUST-1 (0.6 mg cm^{-2})/PTFE. Promoted CO production, for C-C coupling, could be attributed to the increased CO_2 captured by MOF underlayer. When the MOF amount is increased to 1.2 mg cm^{-2}, we obtained a C_2H_4 FE of 33%, albeit with the H_2 FE remained at 10% at a current density of 800 mA cm^{-2} (Figure S9b, Supporting Information). In MOF mass loading of 1.2 mg cm^{-2}, the MOF amount is too high for efficient CO_2 mass transport.

To understand the correlation between the MOF's CO_2 storage/diffusion capability, mass loading, and catalytic activity, we substituted a MOF with higher CO_2 affinity (**SIFSIX**-3-Cu) for HKUST-1 and investigated the CO_2RR performance of **SIFSIX**-3-Cu augmented GDE.[20] It was reported that CO_2 capacity of **SIFSIX**-3-Cu was 2.4 mmol g^{-1}, whereas HKUST-1 exhibited CO_2 capacity of 0.3 mmol g^{-1}.[51] When the mass loading of **SIFSIX**-3-Cu was 0.3 mg cm^{-2}, C_2H_4 FE maintained over 50% up to a current density of 900 mA cm^{-2} at –1.3 V (vs RHE) (Figure 2c). Despite lower MOF content compared to HKUST-1 case, gaseous CO_2RR product distribution of C/Cu/**SIFSIX**-3-Cu (0.3 mg cm^{-2})/PTFE was similar to that of C/Cu/HKUST-1 (0.6 mg cm^{-2})/PTFE (Figure 2b,c). The correlation between the CO_2RR activity and MOF's CO_2 storage capability/mass loading supports the hypothesis of controlling local CO_2 concentration by augmenting MOFs in GDE. Also, we may expect that CO FE increase at high current density region in both C/Cu/HKUST-1/PTFE and C/Cu/**SIFSIX**-3-Cu/PTFE is related to the increased local CO_2 concentration by MOFs and CO_2RR at DPB, TPR. This can be an interesting topic for future study.

We investigated the geometrical aspect of MOF layer in the GDEs by changing its position and uniformity. We began by forming an adlayer of HKUST-1 (0.6 mg cm^{-2}) on Cu/PTFE and achieved a C_2H_4 FE of 56% at 400 mA cm^{-2} (Figure S9c, Supporting Information). However, H_2 FE also increased from 11% to 20%. This might be due to the instability of HKUST-1 when it directly contacts the flowing catholyte in the flow cell.[52] We also sought to form an adlayer composed of carbon black and HKUST-1 mixture on Cu/PTFE. This resulted in a poor C_2H_4 FE of 34% and a high H_2 FE of 33% at 500 mA cm^{-2} (Figure S9d, Supporting Information). We found that a nonuniform MOF layer is formed when we deposit carbon black and HKUST-1 simultaneously (Figure S10, Supporting Information). This nonuniform MOF layer did not provide the needed consistently high local CO_2 concentration to achieve high current density CO_2RR. Taken together, these results suggest that the hierarchy and uniformity of MOF in a GDE are critical to achieving high-rate CO_2-to-C_2H_4 conversion.

We then showcased the concept of MOF-augmented CO_2 availability in a catholyte-free, zero-gap MEA electrolyzer (**Figure 3**).[12,13] This includes an iridium oxide-supported titanium mesh (IrO_x-Ti) as the anode, an anion exchange membrane, and a GDE with the MOF (HKUST-1, **SIFSIX**-3-Cu) of interest as the cathode electrode. We operated the MEA electrolyzer under ambient temperature and pressure. In CO_2RR, humidified CO_2 gas was supplied from the back side of the GDE, whereas 0.1 M $KHCO_3$ was circulated in the anodic chamber (Figure 3a). Recently, it was reported that the protons C_2H_4 are supplied by the aqueous anolyte; and that water in humidified CO_2 increases water activity and affects the GDE microenvironment, providing enhanced CO_2RR kinetics.[42] We studied the effect of MOF layer (mass loading = 0.6 mg cm^{-2}) by varying the MOF position (overlayer or underlayer) in GDE according to 165 nm sputtered Cu since the micro-environment in MEA electrolyzer could be very different from the flow cell during CO_2RR (Figure 3b).

We began with investigating the CO_2RR performance of unmodified Cu/PTFE (Figure 3c). The performance was investigated by gaseous products in CO_2RR of MEA electrolyzers. We noted a gradual decrease in CO FE from 74% to 17% and a gradual increase in C_2H_4 FE from 11% to 43% with the full-cell potential increasing from –3 to –3.8 V. At –3.8 V, the system delivered a peak C_2H_4 FE of 42% at a total current density of 175 mA cm^{-2}. We then sought to modify the surface of the Cu/PTFE with an adlayer composed of carbon black and PFSA ionomer—a strategy to improve the C_2H_4 productivities at the expense of increasing applied potential.[12,47] We observed a peak C_2H_4 FE of 54% at a total current density of 400 mA cm^{-2} and at a full-cell potential of –4.0 V (Figure 3d, Figure S11, Supporting Information).

We further studied the effect of MOF layer by varying its hierarchical order with respect to Cu catalyst in the GDE. In the C/Cu/HKUST-1/PTFE, a peak C_2H_4 FE of 54% was achieved at a total current density of 255 mA cm^{-2} and a full-cell potential of –3.8 V (Figure 3e). Herein, we note that the full-cell potential required to achieve peak C_2H_4 FE on C/Cu/HKUST-1/PTFE was lower than that on C/Cu/PTFE. On C/Cu/**SIFSIX**-3-Cu/PTFE, the peak C_2H_4 FE was below 50% (Figure 3f). When the MOF layer was used as the adlayer, increased C_2H_4 FE was observed at higher full cell potentials compared to Cu/PTFE and C/Cu/PTFE. On C/HKUST-1/Cu/PTFE, we noted a gradual increase in C_2H_4 FE as the full-cell potential increased to –4.1 V. At –4.2 V, C/HKUST-1/Cu/PTFE exhibited a C_2H_4 FE of 52%, while the C_2H_4 FE decreased to 45% at –4.2 V in C/Cu/PTFE (Figure 3g). C/**SIFSIX**-3-Cu/Cu/PTFE—compared to C/Cu/**SIFSIX**-3-Cu/PTFE—showed higher C_2H_4 FEs in a wider range of full-cell potentials from –3.4 to –3.8 V (Figure 3h).

© 2022 Wiley-VCH GmbH

15214095, 0, Downloaded from https://onlinelibrary.wiley.com/doi/10.1002/adma.202207088 by University Of Toronto Libraries, Wiley Online Library on [16/11/2022]. See the Terms and Conditions (https://onlinelibrary.wiley.com/terms-and-conditions) on Wiley Online Library for rules of use; OA articles are governed by the applicable Creative Commons License

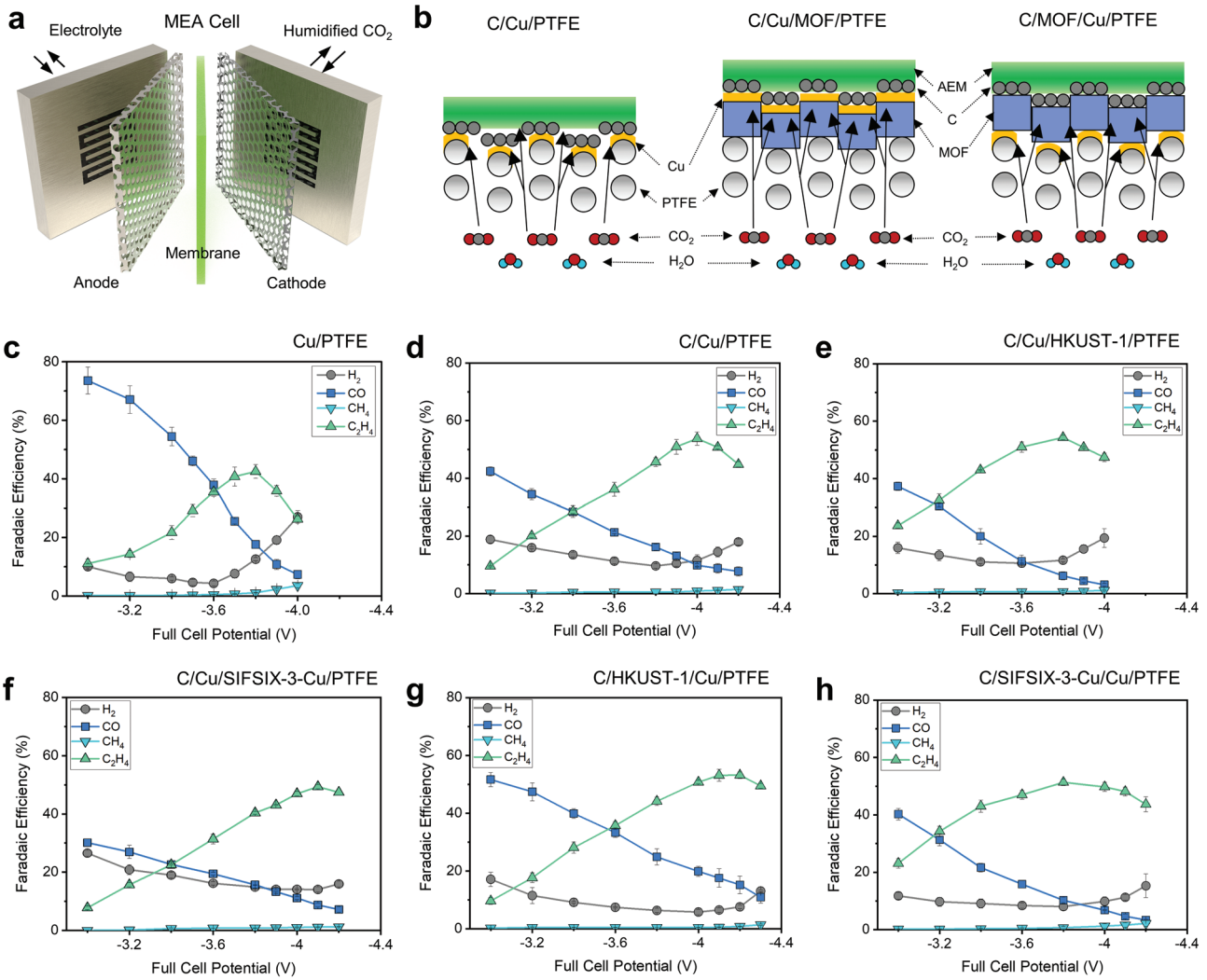

Figure 3. Electrochemical CO_2RR of MOF-augmented GDE in a zero-gap, catholyte-free MEA electrolyzer. a) Components of the CO_2RR MEA electrolyzer. b) Cross-sectional schematic diagram of C/Cu/PTFE, C/Cu/MOF/PTFE, C/MOF/Cu/PTFE which shows the difference in MOF layer position. c–h) CO_2RR FEs in MEA electrolyzer with 0.1 M $KHCO_3$ anolyte according to GDE structure: c) Cu/PTFE, d) C/Cu/PTFE, e) C/Cu/HKUST-1/PTFE, f) C/Cu/**SIFSIX**-3-Cu/PTFE, g) C/HKUST-1/Cu/PTFE, and h) C/**SIFSIX**-3-Cu/Cu/PTFE.

To investigate the CO_2RR activities of GDEs in the MEA electrolyzer, partial current densities of H_2 (J_{H2}), CO (J_{CO}), and C_2H_4 (J_{C2H4}) were compared according to the type of GDEs (**Figure 4**, Figure S12, Supporting Information). In the Cu/PTFE, as the full-cell potential increased over −3.6 V, we noted a rapid increase of J_{H2} and decrease of J_{CO}. A peak J_{C2H4} of 80 mA cm^{-2} was achieved on Cu/PTFE at −3.9 V (Figure 4a–c). Although C/Cu/PTFE promoted the C_2H_4 production with J_{C2H4} of 231 mA cm^{-2} at −4.1 V, a rapid increase of J_{H2} was observed as the potential increased over −3.9 V. As the potential reached −4.2 V, J_{C2H4} decreased to 220 mA cm^{-2} because of elevated HER. Among various GDEs, C/HKUST-1/Cu/PTFE exhibited the lowest J_{H2} at −3.8 V and the highest J_{H2} of C/HKUST-1/Cu/PTFE was only 58 mA cm^{-2} at −4.3 V. In comparison, J_{H2} of C/Cu/PTFE was 88 mA cm^{-2} at −4.2 V. J_{C2H4} of 220 mA cm^{-2} was obtained at −4.3 V on C/HKUST-1/Cu/PTFE—this represents a 2.7-fold improvement in C_2H_4 production rate compared to that of Cu/PTFE (Figure 4c). This is correlated with the highest J_{CO} of C/HKUST-1/Cu/PTFE due to the numerous CO population and promoted *CO dimerization in the high-current-density region. Comparing partial current densities according to the MOF type and position in the MEA electrolyzer, we found that MOFs placed on the sputtered Cu/PTFE were able to suppress the HER and enabled the highest C_2H_4 production rate (Figure S13, Supporting Information).

The working principle of CO_2RR in MEA electrolyzers is similar to that in flow cell: the MOF layer improves CO_2 availability near the catalytic active sites and hence improves C_2H_4 production. Interestingly, when used as the overlayer, the MOF enables higher C_2H_4 production compared to the case where it is used as the underlayer in MEA electrolyzer. This trend is opposite to that observed in alkaline flow cells and may originate from the microenvironment differences between the flow cells and MEA electrolyzers, i.e., the absence of electrolyte, water vapor, and CO_2 supply from the backside of GDE, and site difference where CO_2RR occurs in GDE.

 © 2022 Wiley-VCH GmbH

15214095, 0, Downloaded from https://onlinelibrary.wiley.com/doi/10.1002/adma.202207088 by University Of Toronto Libraries, Wiley Online Library on [16/11/2022]. See the Terms and Conditions (https://onlinelibrary.wiley.com/terms-and-conditions) on Wiley Online Library for rules of use; OA articles are governed by the applicable Creative Commons License

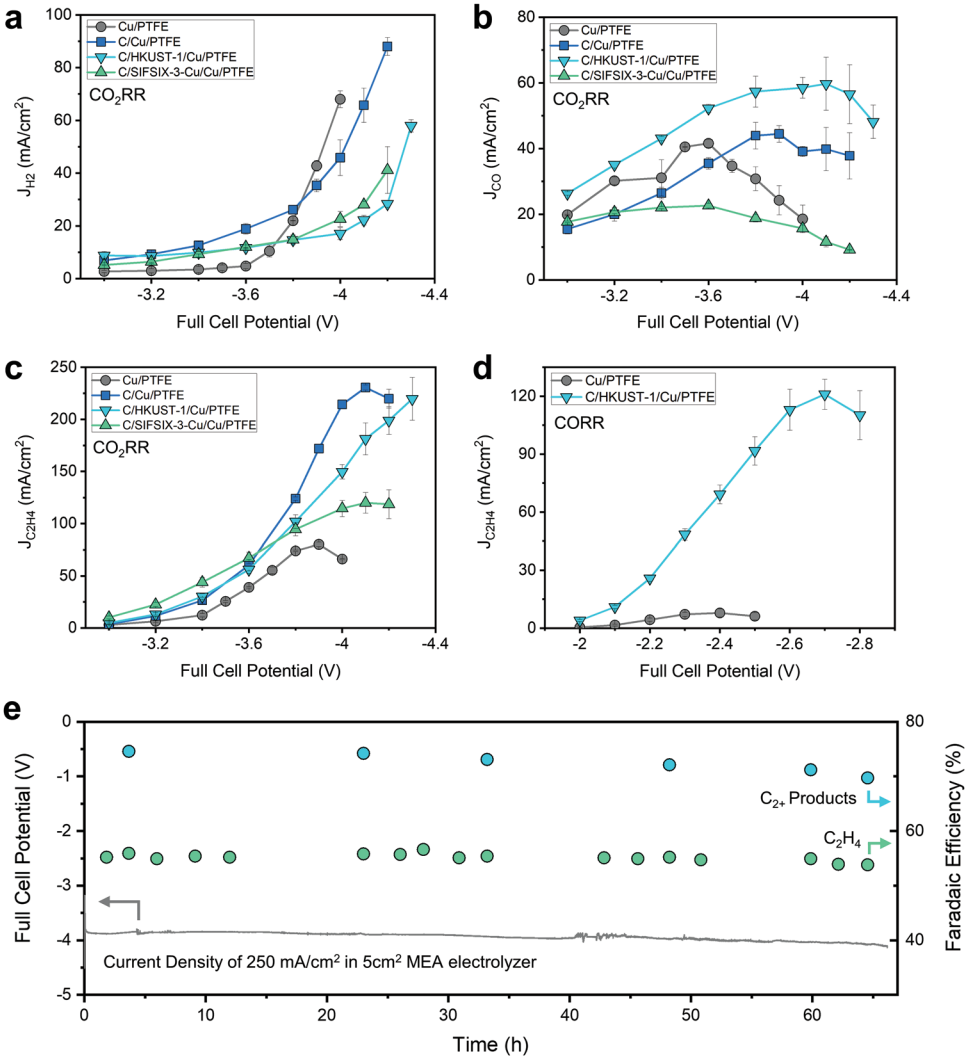

Figure 4. Partial current densities of CO_2RR and CORR versus full cell potential according to GDE structure in an MEA electrolyzer; CO_2RR partial current density comparison between bare GDE and MOF-augmented GDE. a–c) Partial current densities of H_2 (a) CO (b), C_2H_4 (c) in MEA electrolyzer with 0.1 M $KHCO_3$ anolyte, and d) CORR partial current densities of C_2H_4 in MEA electrolyzer with 3 M KOH anolyte. e) CO_2RR stability of C/HKUST-1/Cu/PTFE in MEA electrolyzer with 0.1 M $KHCO_3$ anolyte.

We further extended the application of MOF-augmented GDEs to CORR in MEA electrolyzers with 3 M KOH anolyte (Figure 4d, Figure S14, Supporting Information). In the Cu/PTFE, H_2 was a major CORR product and H_2 FE kept increasing from 37% to 63% as the full cell potential increased to −2.5 V (Figure S14a, Supporting Information). C_2H_4 FE of Cu/PTFE was lower than 17%. However, in the C/HKUST-1/Cu/PTFE, major CORR product was C_2H_4 with the maximum FE of 41% and H_2 FE was lower than 20% until −2.7 V (Figure S14b, Supporting Information). While J_{C2H4} of Cu/PTFE was limited to 8 mA cm^{-2} at −2.4 V, C/HKUST-1/Cu/PTFE exhibited 121 mA cm^{-2} as a maximum J_{C2H4} at −2.7 V (Figure 4d). This reveals that MOF-augmented GDEs with ionomer improve the C_2H_4 production rate by a factor of 15 compared to bare GDE. Higher enhancement of C_2H_4 productivity in CORR compared to CO_2RR might be related to the difference in gas solubility (CO_2 solubility at 10^{-3} M anion concentration: 34×10^{-3} M, CO solubility at 10^{-3} M anion concentration: 0.95×10^{-3} M).[14] This shows that the effect of MOF-augmented GDEs is dominant in the DPB reactions where gas solubility in the electrolyte is low.

The Main CO_2RR products of MOF-augmented GDEs were gas phase (H_2, CO, CH_4, and C_2H_4), and we focused on analyzing gas products in this work (Figure 2, Figure 3). To identify the overall CO_2RR products of C/HKUST-1/Cu/PTFE in MEA electrolyzer, we analyzed liquid products with extra experiments and samples during CO_2RR with the electrolyte of 0.1 M $KHCO_3$ and 1 M KOH. We confirmed that formate, acetate, ethanol, and n-propanol are formed during CO_2RR (Figure S15a and S15b, Supporting Information). We investigated the effect of electrolyte pH by comparing CO_2RR performances of C/HKUST-1/Cu/PTFE in MEA electrolyzers according to the type of electrolyte such as 1 M KOH for alkaline and 0.1 M $KHCO_3$ for neutral (Figure S15, Supporting Information). As the potential increased for high current density, CO FE decreased, and C_2H_4 FE increased by the dimerization of *CO in both cases. When we compared the energy efficiency for ethylene and C_{2+}

 © 2022 Wiley-VCH GmbH

15214095, 0, Downloaded from https://onlinelibrary.wiley.com/doi/10.1002/adma.202207088 by University Of Toronto Libraries, Wiley Online Library on [16/11/2022]. See the Terms and Conditions (https://onlinelibrary.wiley.com/terms-and-conditions) on Wiley Online Library for rules of use; OA articles are governed by the applicable Creative Commons License

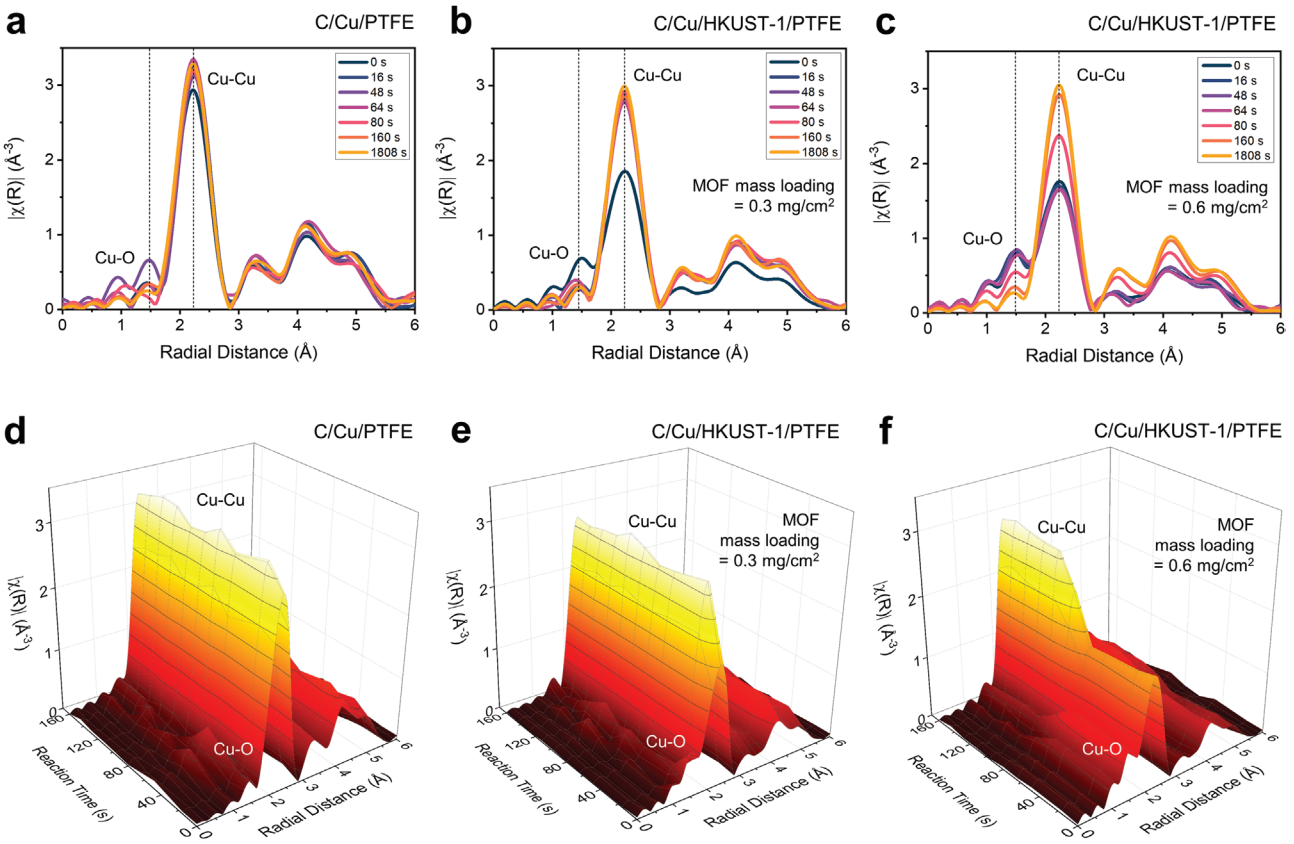

Figure 5. Operando XAS as a function of CO_2RR duration. The operando XAS measurements provide insights into the stability of MOF during CO_2RR. a–c) Comparison of operando Cu-K EXAFS of C/Cu/PTFE (a) and b,c) C/Cu/HKUST-1/PTFE with 0.3 mg cm^{-2} (b) and 0.6 mg cm^{-2} (c) HKUST-1 at a constant CO_2RR current density of 300 mA cm^{-2}. d–f) 3D contour maps of operando EXAFS tracks the changes in Cu–O bonding and Cu–Cu bonding during the reaction time of 0–160 s: d) C/Cu/PTFE and e,f) C/Cu/HKUST-1/PTFE with 0.3 mg cm^{-2} (e) and 0.6 mg cm^{-2} (f) HKUST-1.

products, CO_2RR of C/HKUST-1/Cu/PTFE at 1 M KOH exhibited higher energy efficiency compared to CO_2RR at 0.1 M $KHCO_3$ (Figure S15c and S15d, Supporting Information). Although alkaline electrolytes (KOH) promote the C_2 product formation, reaction with CO_2 and hydroxide ion (OH^-) makes carbonate (CO_3^{2-}).[40,53] This carbonate formation lowers single-path conversion of CO_2 and induces CO_2 input loss. CO_2RR under neutral electrolyte ($KHCO_3$) can mitigate this carbonate formation. Despite the improved CO_2RR activity at lower full cell potentials (higher energy efficiency toward ethylene and C_{2+} products) in alkaline electrolytes, we sought to use neutral electrolytes (0.1 M $KHCO_3$) to mitigate carbonate formation and stable CO_2RR.

The CO_2RR stability of C/HKUST-1/Cu/PTFE was investigated in MEA electrolyzer with 0.1 M $KHCO_3$ anolyte (Figure 4e). At the current density of 250 mA cm^{-2}, C/HKUST-1/Cu/PTFE exhibited superior C_2H_4 production with FE over 50% for 65 h. We further measured FEs for C_{2+} products including ethylene, acetate, ethanol, and n-propanol by analyzing liquid products according to reaction time. Total FEs for C_{2+} products were maintained at over 70% for 59 h.

We investigated the stability of MOFs during CO_2RR (**Figure 5**). We implemented operando XAS analysis of Cu K-edge to track the status of Cu atoms in HKUST-1 during electrochemical reaction. SBU of HKUST-1 is composed of paddle-wheel structured Cu dimer where Cu atoms are coordinated with oxygen (Figure S2, Supporting Information). Thus, studying the Cu K-edge provides information about HKUST-1.[25] Figure 5 shows the operando extended X-ray absorption fine structure (EXAFS) during CO_2RR at a current density of 300 mA cm^{-2} in 1 M KOH electrolyte. Due to Cu reconstruction under reductive potential range of CO_2RR, we detected an increase in the Cu–Cu coordination number (CN) in Cu/PTFE with increasing time of CO_2RR (Figure 5a).[25,26,54] With the HKUST-1 mass loading of 0.3 and 0.6 mg cm^{-2}, Cu–Cu CN of C/Cu/HKUST-1/PTFE before CO_2RR was lower than that of C/Cu/PTFE due to the contribution of Cu atoms in both sputtered Cu and Cu dimers in HKUST-1 (Figure 5b,c).

We compared the operando EXAFS spectra for Cu K edge during CO_2RR (Figure 5d–f). Before CO_2RR, Cu–O CN of C/Cu/HKUST-1/PTFE was higher and Cu–Cu CN was lower than those of C/Cu/PTFE, due to the oxygen-coordinated Cu single atoms in the SBU of HKUST-1 (Figure S2, Supporting Information).[25] During CO_2RR, Cu–Cu CN increased and Cu–O CN decreased, likely due to the reconstruction of the Cu catalyst under reductive potential and the formation of Cu clusters from Cu dimer in HKUST-1.[25] When the mass loading of HKUST-1 was increased to 0.6 mg cm^{-2}, Cu–Cu CN was maintained low until 60 s and then rapidly increased. We found that higher loading of HKUST-1 induces a slower increasing rate

 © 2022 Wiley-VCH GmbH

15214095, 0, Downloaded from https://onlinelibrary.wiley.com/doi/10.1002/adma.202207088 by University Of Toronto Libraries, Wiley Online Library on [16/11/2022]. See the Terms and Conditions (https://onlinelibrary.wiley.com/terms-and-conditions) on Wiley Online Library for rules of use; OA articles are governed by the applicable Creative Commons License

of Cu–Cu CN because it takes more time for reconstruction of Cu dimer at higher mass loading of MOFs. This phenomenon was confirmed by operando X-ray absorption near edge structure (XANES) comparison between C/Cu/PTFE and C/Cu/HKUST-1/PTFE (Figure S16, Supporting Information). XRD of C/Cu/HKUST-1 (0.6 mg cm^{-2})/PTFE supports the reconstruction of HKUST-1 (Figure S17, Supporting Information). When we analyzed XRD of C/HKUST-1/Cu/PTFE, we found a decrease of (220) and (222) XRD peaks for HKUST-1 after CORR in the flow cell with 3 M KOH (Figure S18, Supporting Information). This reveals that Cu reconstruction in MOFs can be induced by not only CO_2RR, but also CORR. Therefore, MOF-induced organic layers, formed by the reconstruction of Cu in SBU, contribute to the CO_2 adsorption and the control of local CO_2 concentration, which enables high current density CO_2RR in MOF-augmented GDEs.

To investigate the role of MOF underlayer with other metal-based MOFs, we synthesized ZIF-8 with Zn centers (Figure S19, Supporting Information). When we investigated the CO_2RR of ZIF-8 on carbon paper, formate ($HCOO^-$) was the main product. As the current density increased from 200 to 600 mA cm^{-2}, H_2 FE increased from 5 to 8%, and $HCOO^-$ FE decreased from 81 to 65% (Figure S19e, Supporting Information). However, when the ZIF-8 layer was incorporated between sputtered Cu and PTFE (C/Cu/ZIF-8/PTFE), the H_2 FE was less than 3% and $HCOO^-$ FE was 88% at 600 mA cm^{-2} (Figure S19f, Supporting Information). It means that Zn-based MOF underlayer also shows enhanced CO_2 mass transport and high-rate CO_2RR for $HCOO^-$ production. We confirmed that MOF layers in GDE can have a bifunctional effect on CO_2RR as: (1) increasing local CO_2 concentration by MOF-induced organic layer, and (2) acting as CO_2RR active sites by metallic species in MOFs.

3. Conclusion

We present MOF-modified GDEs that enable selective and high-rate CO_2-to-C_2H_4 conversion in the flow cell and MEA electrolyzers. The design principle relies on pre-concentration of the CO_2 near the catalytically active sites via CO_2-absorbing MOF-induced organic layers as the adlayer or underlayer depending on the electrolyzer configuration. Implementing this strategy in flow cell electrolyzers, we achieved a C_2H_4 FE of 49% and an H_2 FE of 11% at current densities of 1 A cm^{-2}. We successfully translated the concept to neutral media MEA electrolyzers and achieved a C_2H_4 FE of 52% at a full-cell potential of –4.2 V. J_{C2H4} as high as 220 mA cm^{-2} was achieved at –4.3 V, representing a 2.7-fold enhanced C_2H_4 productivity compared to that of Cu/PTFE (80 mA cm^{-2} at –3.9 V). For CORR, where gas solubility in the electrolyte is lower than CO_2RR, MOF-augmented GDEs exhibited J_{C2H4} of 121 mA cm^{-2} at –2.7 V, 15-fold higher than that of bare GDE. Operando EXAFS analysis of MOF-augmented GDE during CO_2RR reveals the reconstruction of Cu atoms in MOFs to form Cu clusters with MOF-induced organic layers, which promotes the current density in CO_2RR. We found a correlation between CO_2 capture ability (HKUST-1, **SIFSIX**-3-Cu) and mass loading of MOFs with CO_2RR activities. It was revealed that the CO_2 capture ability of MOF can be transferred to MOF-induced organic layers with Cu clusters. The phenomena presented herein showcase electrode design principles that are not limited by prior local CO_2 availability obstacles. The MOF-augmented GDEs pave the way to the realization of renewable electrosynthesis of ethylene: the world's most produced chemical.

4. Experimental Section

Synthesis of HKUST-1: HKUST-1 ($Cu_3(btc)_2{\cdot}xH_2O$, btc = benzene-1,3,5-tricarboxylate) was fabricated using the reaction between Cu nitrate ($Cu(NO_3)_2$) solution and benzene-1,3,5-tricarboxylic acid ($C_9H_6O_6$) solution. Cu nitrate containing methanol solution (50 mL) was mixed with 50 mL benzene-1,3,5-tricarboxylic acid at room temperature and the mixed solution was stirred for the HKUST-1 formation. The resulting solution was washed by centrifuge and mixing with methanol. The washed HKUST-1 was dried in a vacuum oven overnight. Activation of HKUST-1 was proceeded by the calcination at 250 °C.[25]

Synthesis of **SIFSIX**-*3-Cu MOFs*: The **SIFSIX**-3-Cu MOF was synthesized by layering a methanolic solution of pyrazine onto a methanolic of $CuSiF_6 \times H_2O$ solution. Upon this layering, a fast formation of light violet powder was perceived, which was left for 24 h in the solution. The powder was collected and washed with methanol, then dried under vacuum 85 °C overnight and characterized using powder XRD (PXRD) (Figure S4, Supporting Information). The PXRD diagram of **SIFSIX**-3-Cu in this work is found to match with that of the structure studied in the previous report.[20] Activation of **SIFSIX**-3-Cu was proceeded by the calcination at 100 °C.

Synthesis of ZIF-8 MOFs: Pristine ZIF-8 was synthesized by mixing metal precursor solution and ligand solution.[55] 1.37 g of zinc acetate ($Zn(Ac){\cdot}2H_2O$, 6.25 mmol) was dissolved in 50 mL methanol. 2.05 g of 2-methylimidazole (2-MeI, 25 mmol) was dissolved in 50 mL methanol. After mixing metal precursor and ligand solution, the mixed solution was stirred for 10 h in room temperature. It was washed three times with methanol and dried in a vacuum oven at 50 °C overnight. 100 mg of as-synthesized ZIF-8 was calcined at 240°C for 3 h in ambient air condition.

Fabrication of GDE: Cu/PTFE was fabricated by sputtering 300 nm Cu onto a PTFE substrate, and C/Cu/PTFE was fabricated by spray-coating an ink containing carbon black powder and Nafion binder (D520 Nafion, 1000 EW) on the Cu/PTFE. For the MOF-augmented GDE fabrication, MOF powder-dispersed ink containing Nafion binder (D520 Nafion, 1000 EW) and methanol was spray-coated, and the mass loading of MOFs was varied between 0.3 and 1.2 mg cm^{-2}. For the flow cell experiment, the thickness of Cu was 300 nm. For the MEA electrolyzer experiment, the thickness of Cu was 165 nm.

Material Characterization: XRD analysis of MOFs and MOF-augmented GDEs was carried out with a Rigaku MiniFlex 600 diffractometer using Cu Kα radiation (λ = 1.54 Å). Hitachi FE-SEM S-5200 was used for SEM analysis. Operando XAS of Cu K edge was analyzed at 9 BM of Advanced Photon Source (APS) in Arbonne National Laboratory. Operando XAS was carried at flow cell type reactor with the current density of 300 mA cm^{-2} in 1 M KOH electrolyte.

Electrochemical CO_2 Reduction: CO_2RR activities of MOF-augmented GDEs were measured by potentiostat and current booster (Autolab) with flow cell and MEA electrolyzer. For the CO_2RR of flow cell, nickel foam, anion exchange membrane, and MOF-augmented GDEs were used. PTFE was used with the pore size of 0.45 µm for all GDEs fabrication, which had merit of high CO production and conversion to C_2H_4 in the CO_2RR of Cu/HKUST-1/PTFE (Figure S20, Supporting Information). 1 M KOH was flowed in the cathode and anode chamber, separated by anion exchange membrane (Fumasep FAA-3-PK-130). CO_2 with controlled flow rate of 50 sccm was supplied from the backside of the GDE in the flow cell. The outlet gas flow rate was measured from the electrolyzer to calculate the FE of CO_2RR products. Ag/AgCl (3 M KCl) potentials were converted to RHE based on $E_{RHE} = E_{Ag/AgCl} + 0.210 + 0.059 \times pH$ with

© 2022 Wiley-VCH GmbH

15214095, 0, Downloaded from https://onlinelibrary.wiley.com/doi/10.1002/adma.202207088 by University Of Toronto Libraries, Wiley Online Library on [16/11/2022]. See the Terms and Conditions (https://onlinelibrary.wiley.com/terms-and-conditions) on Wiley Online Library for rules of use; OA articles are governed by the applicable Creative Commons License

iR correction. For the CO_2RR of MEA electrolyzer, cathode, anode flow fields were used with the active area of 5 cm^2. Iridium-oxide-supported titanium mesh (IrOx-Ti) was used as the anode, an anion exchange membrane (Sustainion X37-50), and a GDE as the cathode electrode. The cell was operated under ambient temperature and pressure. Humidified CO_2 (g) was supplied from the back side of the cathode, and 0.1 M $KHCO_3$ was circulated in the anode part. Gas products of CO_2RR were analyzed by gas chromatography (GC, Perkin Elmer Clarus 600). Thermal conductivity detector (TCD) + a flame ionization detector (FID) in GC analyzed H_2, CO, CH_4, and C_2H_4. The gas products of CO_2RR were collected from the cathodic product stream in 1 mL volumes via gas chromatography syringes. The samples were then injected into the GC. To analyze liquid products, ^{1}H NMR spectroscopy (Agilent DD2 600 MHz) was used using dimethyl sulfoxide (DMSO) as internal standard (Figure S15, Supporting Information). For the CORR of MEA electrolyzers, 3 M KOH was used as an electrolyte for the anode, and humidified CO (g) was supplied to the cathode.

Supporting Information

Supporting Information is available from the Wiley Online Library or from the author.

Acknowledgements

D.-H.N., O.S., and A.O. contributed equally to this work. This publication is based upon work supported by the King Abdullah University of Science and Technology (KAUST) Office of Sponsored Research (OSR) under Award No. OSR-2018-CPF-3665-03. This work was supported by the National Research Foundation of Korea (NRF) grant funded by the Korean government (MSIT) (NRF-2020R1F1A1077411). This research was supported by the program of Carbon to X technology development for the production of useful substances (NRF-2020M3H7A1098376), through the National Research Foundation of Korea (NRF), funded by the Korean government (Ministry of Science and ICT (MSIT)).

Conflict of Interest

The authors declare no conflict of interest.

Data Availability Statement

The data that support the findings of this study are available from the corresponding author upon reasonable request.

Keywords

electrochemical CO_2 reduction, ethylene production, gas-diffusion electrodes, metal–organic frameworks, reticular chemistry

Received: August 4, 2022
Revised: October 3, 2022
Published online:

[1] P. De Luna, C. Hahn, D. Higgins, S. A. Jaffer, T. F. Jaramillo, E. H. Sargent, *Science* **2019**, *364*, eaav3506.
[2] R. I. Masel, Z. Liu, H. Yang, J. J. Kaczur, D. Carrillo, S. Ren, D. Salvatore, C. P. Berlinguette, *Nat. Nanotechnol.* **2021**, *16*, 118.
[3] D. Bagchi, J. Raj, A. K. Singh, A. Cherevotan, S. Roy, K. S. Manoj, C. P. Vinod, S. C. Peter, *Adv. Mater.* **2022**, *34*, 2109426.
[4] A. Ozden, F. Li, F. P. García de Arquer, A. Rosas-Hernández, A. Thevenon, Y. Wang, S.-F. Hung, X. Wang, B. Chen, J. Li, J. Wicks, M. Luo, Z. Wang, T. Agapie, J. C. Peters, E. H. Sargent, D. Sinton, *ACS Energy Lett.* **2020**, *5*, 2811.
[5] M. Jouny, W. Luc, F. Jiao, *Ind. Eng. Chem. Res.* **2018**, *57*, 2165.
[6] J. Sisler, S. Khan, A. H. Ip, M. W. Schreiber, S. A. Jaffer, E. R. Bobicki, C.-T. Dinh, E. H. Sargent, *ACS Energy Lett.* **2021**, *6*, 997.
[7] J. Na, B. Seo, J. Kim, C. W. Lee, H. Lee, Y. J. Hwang, B. K. Min, D. K. Lee, H.-S. Oh, U. Lee, *Nat. Commun.* **2019**, *10*, 5193.
[8] M. G. Kibria, J. P. Edwards, C. M. Gabardo, C.-T. Dinh, A. Seifitokaldani, D. Sinton, E. H. Sargent, *Adv. Mater.* **2019**, *31*, 1807166.
[9] H. Shin, K. U. Hansen, F. Jiao, *Nat. Sustain.* **2021**, *4*, 911.
[10] M. B. Ross, P. De Luna, Y. Li, C.-T. Dinh, D. Kim, P. Yang, E. H. Sargent, *Nat. Catal.* **2019**, *2*, 648.
[11] D. Higgins, C. Hahn, C. Xiang, T. F. Jaramillo, A. Z. Weber, *ACS Energy Lett.* **2019**, *4*, 317.
[12] C. M. Gabardo, C. P. O'Brien, J. P. Edwards, C. McCallum, Y. Xu, C.-T. Dinh, J. Li, E. H. Sargent, D. Sinton, *Joule* **2019**, *3*, 2777.
[13] F. Li, A. Thevenon, A. Rosas-Hernández, Z. Wang, Y. Li, C. M. Gabardo, A. Ozden, C. T. Dinh, J. Li, Y. Wang, J. P. Edwards, Y. Xu, C. McCallum, L. Tao, Z.-Q. Liang, M. Luo, X. Wang, H. Li, C. P. O'Brien, C.-S. Tan, D.-H. Nam, R. Quintero-Bermudez, T.-T. Zhuang, Y. C. Li, Z. Han, R. D. Britt, D. Sinton, T. Agapie, J. C. Peters, E. H. Sargent, *Nature* **2020**, *577*, 509.
[14] F. P. García de Arquer, C.-T. Dinh, A. Ozden, J. Wicks, C. McCallum, A. R. Kirmani, D.-H. Nam, C. Gabardo, A. Seifitokaldani, X. Wang, Y. C. Li, F. Li, J. Edwards, L. J. Richter, S. J. Thorpe, D. Sinton, E. H. Sargent, *Science* **2020**, *367*, 661.
[15] J. Wicks, M. L. Jue, V. A. Beck, J. S. Oakdale, N. A. Dudukovic, A. L. Clemens, S. Liang, M. E. Ellis, G. Lee, S. E. Baker, E. B. Duoss, E. H. Sargent, *Adv. Mater.* **2021**, *33*, 2003855.
[16] N. T. Nesbitt, T. Burdyny, H. Simonson, D. Salvatore, D. Bohra, R. Kas, W. A. Smith, *ACS Catal.* **2020**, *10*, 14093.
[17] T. Moore, X. Xia, S. E. Baker, E. B. Duoss, V. A. Beck, *ACS Energy Lett.* **2021**, *6*, 3600.
[18] M. Younas, M. Rezakazemi, M. Daud, M. B. Wazir, S. Ahmad, N. Ullah, S. R. Inamuddin, *Prog. Energy Combust. Sci.* **2020**, *80*, 100849.
[19] J.-S. Qin, S. Yuan, A. Alsalme, H.-C. Zhou, *ACS Appl. Mater. Interfaces* **2017**, *9*, 33408.
[20] O. Shekhah, Y. Belmabkhout, Z. Chen, V. Guillerm, A. Cairns, K. Adil, M. Eddaoudi, *Nat. Commun.* **2014**, *5*, 4228.
[21] I. Skarmoutsos, Y. Belmabkhout, K. Adil, M. Eddaoudi, G. Maurin, *J. Phys. Chem. C* **2017**, *121*, 27462.
[22] O. Shekhah, Y. Belmabkhout, K. Adil, P. M. Bhatt, A. J. Cairns, M. Eddaoudi, *Chem. Commun.* **2015**, *51*, 13595.
[23] Y. Belmabkhout, P. M. Bhatt, K. Adil, R. S. Pillai, A. Cadiau, A. Shkurenko, G. Maurin, G. Liu, W. J. Koros, M. Eddaoudi, *Nat. Energy* **2018**, *3*, 1059.
[24] V. Chernikova, O. Shekhah, Y. Belmabkhout, M. Eddaoudi, *ACS Appl. Nano Mater.* **2020**, *3*, 6432.
[25] D.-H. Nam, O. S. Bushuyev, J. Li, P. De Luna, A. Seifitokaldani, C.-T. Dinh, F. P. García de Arquer, Y. Wang, Z. Liang, A. H. Proppe, C. S. Tan, P. Todorovic, O. Shekhah, C. M. Gabardo, J. W. Jo, J. Choi, M.-J. Choi, S.-W. Baek, J. Kim, D. Sinton, S. O. Kelley, M. Eddaoudi, E. H. Sargent, *J. Am. Chem. Soc.* **2018**, *140*, 11378.
[26] Z. Weng, Y. Wu, M. Wang, J. Jiang, K. Yang, S. Huo, X.-F. Wang, Q. Ma, G. W. Brudvig, V. S. Batista, Y. Liang, Z. Feng, H. Wang, *Nat. Commun.* **2018**, *9*, 415.
[27] H. Jiang, Q. He, Y. Zhang, L. Song, *Acc. Chem. Res.* **2018**, *51*, 2968.
[28] X.-F. Qiu, H.-L. Zhu, J.-R. Huang, P.-Q. Liao, X.-M. Chen, *J. Am. Chem. Soc.* **2021**, *143*, 7242.

 © 2022 Wiley-VCH GmbH

15214095, 0, Downloaded from https://onlinelibrary.wiley.com/doi/10.1002/adma.202207088 by University Of Toronto Libraries, Wiley Online Library on [16/11/2022]. See the Terms and Conditions (https://onlinelibrary.wiley.com/terms-and-conditions) on Wiley Online Library for rules of use; OA articles are governed by the applicable Creative Commons License

[29] Y. Liu, S. Li, L. Dai, J. Li, J. Lv, Z. Zhu, A. Yin, P. Li, B. Wang, *Angew. Chem., Int. Ed.* **2021**, *60*, 16409.
[30] S. Nitopi, E. Bertheussen, S. B. Scott, X. Liu, A. K. Engstfeld, S. Horch, B. Seger, I. E. L. Stephens, K. Chan, C. Hahn, J. K. Nørskov, T. F. Jaramillo, I. Chorkendorff, *Chem. Rev.* **2019**, *119*, 7610.
[31] Y. Wang, H. Shen, K. J. T. Livi, D. Raciti, H. Zong, J. Gregg, M. Onadeko, Y. Wan, A. Watson, C. Wang, *Nano Lett.* **2019**, *19*, 8461.
[32] J. Zhang, W. Luo, A. Züttel, *J. Mater. Chem. A* **2019**, *7*, 26285.
[33] W. Liu, P. Zhai, A. Li, B. Wei, K. Si, Y. Wei, X. Wang, G. Zhu, Q. Chen, X. Gu, R. Zhang, W. Zhou, Y. Gong, *Nat. Commun.* **2022**, *13*, 1877.
[34] M. Zhong, K. Tran, Y. Min, C. Wang, Z. Wang, C.-T. Dinh, P. De Luna, Z. Yu, A. S. Rasouli, P. Brodersen, S. Sun, O. Voznyy, C.-S. Tan, M. Askerka, F. Che, M. Liu, A. Seifitokaldani, Y. Pang, S.-C. Lo, A. Ip, Z. Ulissi, E. H. Sargent, *Nature* **2020**, *581*, 178.
[35] F. Li, A. Thevenon, A. Rosas-Hernández, Z. Wang, Y. Li, C. M. Gabardo, A. Ozden, C. T. Dinh, J. Li, Y. Wang, J. P. Edwards, Y. Xu, C. McCallum, L. Tao, Z.-Q. Liang, M. Luo, X. Wang, H. Li, C. P. O'Brien, C.-S. Tan, D.-H. Nam, R. Quintero-Bermudez, T.-T. Zhuang, Y. C. Li, Z. Han, R. D. Britt, D. Sinton, T. Agapie, J. C. Peters, E. H. Sargent, *Nature* **2019**, *577*, 509.
[36] S. Sultan, H. Lee, S. Park, M. M. Kim, A. Yoon, H. Choi, T.-H. Kong, Y.-J. Koe, H.-S. Oh, Z. Lee, H. Kim, W. Kim, Y. Kwon, *Energy Environ. Sci.* **2022**, *15*, 2397.
[37] Z. Xing, L. Hu, D. S. Ripatti, X. Hu, X. Feng, *Nat. Commun.* **2021**, *12*, 136.
[38] X. Chen, J. Chen, N. M. Alghoraibi, D. A. Henckel, R. Zhang, U. O. Nwabara, K. E. Madsen, P. J. A. Kenis, S. C. Zimmerman, A. A. Gewirth, *Nat. Catal.* **2021**, *4*, 20.
[39] G. Zhang, Z.-J. Zhao, D. Cheng, H. Li, J. Yu, Q. Wang, H. Gao, J. Guo, H. Wang, G. A. Ozin, T. Wang, J. Gong, *Nat. Commun.* **2021**, *12*, 5745.
[40] A. Ozden, F. P. García de Arquer, J. E. Huang, J. Wicks, J. Sisler, R. K. Miao, C. P. O'Brien, G. Lee, X. Wang, A. H. Ip, E. H. Sargent, D. Sinton, *Nat. Sustain.* **2022**, *5*, 563.
[41] G. O. Larrazábal, V. Okatenko, I. Chorkendorff, R. Buonsanti, B. Seger, *ACS Appl. Mater. Interfaces* **2022**, *14*, 7779.
[42] W. Choi, S. Park, W. Jung, D. H. Won, J. Na, Y. J. Hwang, *ACS Energy Lett.* **2022**, *7*, 939.
[43] D.-H. Nam, P. De Luna, A. Rosas-Hernández, A. Thevenon, F. Li, T. Agapie, J. C. Peters, O. Shekhah, M. Eddaoudi, E. H. Sargent, *Nat. Mater.* **2020**, *19*, 266.
[44] M. Ding, R. W. Flaig, H.-L. Jiang, O. M. Yaghi, *Chem. Soc. Rev.* **2019**, *48*, 2783.
[45] H. Zhong, M. Ghorbani-Asl, K. H. Ly, J. Zhang, J. Ge, M. Wang, Z. Liao, D. Makarov, E. Zschech, E. Brunner, I. M. Weidinger, J. Zhang, A. V. Krasheninnikov, S. Kaskel, R. Dong, X. Feng, *Nat. Commun.* **2020**, *11*, 1409.
[46] C. S. Diercks, Y. Liu, K. E. Cordova, O. M. Yaghi, *Nat. Mater.* **2018**, *17*, 301.
[47] C.-T. Dinh, T. Burdyny, M. G. Kibria, A. Seifitokaldani, C. M. Gabardo, F. P. García de Arquer, A. Kiani, J. P. Edwards, P. De Luna, O. S. Bushuyev, C. Zou, R. Quintero-Bermudez, Y. Pang, D. Sinton, E. H. Sargent, *Science* **2018**, *360*, 783.
[48] K. Yang, R. Kas, W. A. Smith, T. Burdyny, *ACS Energy Lett.* **2021**, *6*, 33.
[49] M. Todaro, G. Buscarino, L. Sciortino, A. Alessi, F. Messina, M. Taddei, M. Ranocchiari, M. Cannas, F. M. Gelardi, *J. Phys. Chem. C* **2016**, *120*, 12879.
[50] Y. C. Tan, K. B. Lee, H. Song, J. Oh, *Joule* **2020**, *4*, 1104.
[51] W. Liang, P. M. Bhatt, A. Shkurenko, K. Adil, G. Mouchaham, H. Aggarwal, A. Mallick, A. Jamal, Y. Belmabkhout, M. Eddaoudi, *Chem* **2019**, *5*, 950.
[52] J. R. Álvarez, E. Sánchez-González, E. Pérez, E. Schneider-Revueltas, A. Martínez, A. Tejeda-Cruz, A. Islas-Jácome, E. González-Zamora, I. A. Ibarra, *Dalton Trans.* **2017**, *46*, 9192.
[53] H. Xiao, T. Cheng, W. A. Goddard, R. Sundararaman, *J. Am. Chem. Soc.* **2016**, *138*, 483.
[54] J. Li, F. Che, Y. Pang, C. Zou, J. Y. Howe, T. Burdyny, J. P. Edwards, Y. Wang, F. Li, Z. Wang, P. De Luna, C.-T. Dinh, T.-T. Zhuang, M. I. Saidaminov, S. Cheng, T. Wu, Y. Z. Finfrock, L. Ma, S.-H. Hsieh, Y.-S. Liu, G. A. Botton, W.-F. Pong, X. Du, J. Guo, T.-K. Sham, E. H. Sargent, D. Sinton, *Nat. Commun.* **2018**, *9*, 4614.
[55] Y. Wang, P. Hou, Z. Wang, P. Kang, *ChemPhysChem* **2017**, *18*, 3142.

© 2022 Wiley-VCH GmbH

15214095, 0, Downloaded from https://onlinelibrary.wiley.com/doi/10.1002/adma.202207088 by University Of Toronto Libraries, Wiley Online Library on [16/11/2022]. See the Terms and Conditions (https://onlinelibrary.wiley.com/terms-and-conditions) on Wiley Online Library for rules of use; OA articles are governed by the applicable Creative Commons License